

Understanding Cellular Noise with Optical Perturbation and Deep Learning

Chuanbo Liu¹, Yu Fu^{1,2}, Lu Lin^{1,2}, Elliot L. Elson^{3,†}, and Jin Wang^{4,‡}

¹State Key Laboratory of Electroanalytical Chemistry, Changchun Institute of Applied Chemistry, Chinese Academy of Sciences, Changchun, Jilin, 130022, P.R. China.

²University of Chinese Academy of Sciences, Beijing, 100000, P.R. China.

³Department of Biochemistry and Molecular Biophysics, Washington University in St. Louis, Saint Louis, MO 63130, United States.

⁴Department of Chemistry and of Physics and Astronomy, State University of New York, Stony Brook, New York, 11794-3400, United States.

[†]elson@wustl.edu

[‡]jin.wang.1@stonybrook.edu

Abstract

Noise plays a crucial role in the regulation of cellular and organismal function and behavior. Exploring noise's impact is key to understanding fundamental biological processes, such as gene expression, signal transduction, and the mechanisms of development and evolution. Currently, a comprehensive method to quantify dynamical behavior of cellular noise within these biochemical systems is lacking. In this study, we introduce an optically-controlled perturbation system utilizing the light-sensitive Phytochrome B (PhyB) from *Arabidopsis thaliana*, which enables precise noise modulation with high spatial-temporal resolution. Our system exhibits exceptional sensitivity to light, reacting consistently to pulsed light signals, distinguishing it from other photoreceptor-based promoter systems that respond to a single light wavelength. To characterize our system, we developed a stochastic model for phytochromes that accounts for photoactivation/deactivation, thermal reversion, and the dynamics of the light-activated gene promoter system. To precisely control our system, we determined the rate constants for this model using an omniscient deep neural network that can directly map rate constant combinations to time-dependent state joint distributions. By adjusting the activation rates through light intensity and degradation rates via N-terminal mutagenesis, we illustrate that our optical-controlled perturbation can effectively modulate molecular expression level as well as noise. Our results highlight the potential of employing an optically-controlled gene perturbation system as a noise-controlled stimulus source. This approach, when combined with the analytical capabilities of a sophisticated deep neural network, enables the accurate estimation of rate constants from observational data in a broad range of biochemical reaction networks.

Introduction

In fully differentiated cells under constant environmental conditions, the morphology, function, and number of cell-specific organelles, as well as the capacity for cell-to-cell communication, the potential for interaction with extracellular molecules, and the function-specific metabolic adaptations, among other characteristics, appear unchanged from a macroscopic perspective, suggesting a stable cell state. On the other hand, cell state diversity is frequently observed through single-cell and single-molecule techniques¹. Given that the features of a cell are defined by its molecular composition, it is reasonable to postulate that the number of molecules of proteins, including enzymes, structural proteins, and signaling molecules, fluctuate around a constant mean in a stable cell state. These fluctuations are attributed to both intrinsic and extrinsic sources of noise². It is generally assumed that the magnitude of noise remains consistent over time in a constant environment, leading to a steady-state distribution. Furthermore, the distinct difference of living cell to a thermal equilibrium system is the exchange of both energy and materials with the environment at a constant rate apart from stochastic fluctuations to maintain the steady-state. From a thermodynamic perspective, a living cell in this circumstance is characterized as a non-equilibrium steady-state (NESS)³.

The ability to reach and maintain NESS hinges critically on the chemical and thermal equilibrium of the biochemical reactions within the cell, which defines the phenotype of the cell. Conversely, a cell's response to external stimuli is contingent upon the dynamics of signaling components, which encodes vital biological information for the cell^{4,5}. Consequently, the cellular response to external stimuli is regulated not solely by the steady-state concentrations of various species but also by the dynamics, which are characterized by both the instantaneous numbers of molecules and their spatial distributions. Thus, to thoroughly understand the behavior of biochemical systems, it is imperative to quantify not just the mean populations of molecules but, more critically, the temporal variations and spatial heterogeneity in the distributions of cellular states.

Although significant progress has been made in understanding the noise of cells in slowly-changing environments⁶⁻⁹, the dynamics induced by rapidly-evolving or spatially-specific perturbations remain poorly understood. One of the primary challenges is the development of efficient labeling techniques for molecular species that enable high-throughput tracking and precise quantification. A further, and perhaps more critical, challenge is the absence of high-resolution spatio-temporal modulation methods capable of generating or simulating rapid spatio-temporal stimuli for cellular reaction networks. The first challenge has been largely addressed through the use of efficient single-molecule hybridization/tagging techniques or deep sequencing^{1,10,11}. While the second challenge may be surmountable by harnessing optogenetic technologies. Over recent decades, optogenetics has emerged as a pivotal technique for exerting precise spatio-temporal control in cells, with applications in neu-

rosience, cell physiology, and cardiology¹²⁻¹⁶. Employing a synergistic approach of genetic engineering and bioorthogonal light, which is independent of the native cellular chemical reactions, both natural and synthetic photoreceptors can be utilized to modulate the activity of targeted cells within a highly heterogeneous tissue matrix. The specificity of expression and subcellular localization within the host organism is facilitated through the incorporation of regulatory elements such as promoters, enhancers, and precise targeting sequences into the photoreceptor-encoding DNA constructs. Consequently, cells that are intrinsically non-responsive to light can be rendered photosensitive, thereby becoming amenable to spatially and temporally precise control via targeted illumination.

However, mapping the dynamic properties of biological systems remains challenging, despite the availability of precise spatial-temporal perturbation control. From a modeling perspective, constructing a detailed model for gene expression regulated by light is arduous. The challenge arises because the rate constants are intertwined with cell-state variables, such as the populations of RNA polymerase (RNAP) and ribosomes¹⁷, the levels of transcription factors and micro-RNAs¹⁸, the binding affinities of genes with RNAP and transcription factors¹⁹, gene copy numbers²⁰, the phase of the cell cycle²¹, nutrient density²², and chromosomal conformations²³, among others. These latent variables, typically unmeasured in biochemical experiments, are considered intrinsic noise, in contrast to extrinsic noise, which is induced by the influence of changing environments. The interaction between the control protocol and cell states, modulated by these latent variables, adds further complexity to the modeling of the system.

On the other hand, gene expression is an intricate complex chemical reaction system involving the binding of transcription factors to DNA regulatory sequences, recruitment of RNA polymerase, synthesis of nascent mRNAs, modification of these mRNAs, transport of mRNAs from the nucleus to the cytoplasm, and ultimately, the translation of mRNAs in ribosomes²⁴. Each of these processes comprises numerous elementary steps, potentially ranging into the tens or hundreds²⁵⁻²⁸. Many of these elementary steps remain poorly understood, either due to the limitations of current technology rendering them invisible or because they occur at extremely rapid rates^{29,30}. Furthermore, acquiring accurate reaction rates for these elementary steps is particularly challenging. Owing to these complexities, coarse-grained models have been proposed to simulate the gene expression process. Such models employ thermodynamic principles, Boolean logic, and differential equations to deterministically or stochastically represent gene expression, each with varying degrees of computational efficiency and precision^{31,32}. In these models, gene expression is commonly conceptualized as either a one-state or two-state chemical reaction system. Transitions between states, as well as transcription and translation, are often abstracted into effective complex reactions, each encompassing multiple elementary steps³³. While ordinary differential equations can provide reasonable estimates of mean population levels, a stochastic framework

offers a more comprehensive approach. This methodology not only yields insights into the statistical properties of the system but also generates the population distribution, which is crucial for understanding the variability inherent in gene expression systems^{34,35}.

Furthermore, since stochastic modeling is indispensable, another emerging challenge is the inferencing of the rate constants, especially for systems with many species where the state space expands exponentially. This vast state space precludes the possibility of ergodic integration of the system. To address this challenge, Monte Carlo methods are often utilized due to their computational complexity, which is not contingent on the dimensionality of the state space^{36–38}. Despite this, the computational burden remains substantial. The timescale for an exact one-step simulation of biochemical reaction networks is typically on the order of milliseconds, whereas meaningful phenotypic changes occur over hours or days. Consequently, simulating a single trajectory requires the accumulation of millions of Monte Carlo steps. In addition, constructing the posterior distribution necessitates sampling millions to trillions of trajectories, each corresponding to different sets of rate constants. Even with advanced algorithms and hardware that facilitate efficient parallel Monte Carlo sampling, inferring rate constants remains a formidable task, particularly in biological systems with a large number of species.

In this study, we developed an optically-controlled gene expression system utilizing the light-sensitive Phytochrome B (PhyB) from *Arabidopsis thaliana*, engineered for enhanced spatial-temporal precision to probe the intrinsic noise within cellular environments. Our system exhibits a continuous response to pulsed light signals, distinguishing it from previously described blue light-regulated gene expression systems^{39,40}. To broaden the applicability of our system across various biochemical reaction networks, we constructed a stochastic model for phytochromes and an integrated model for the entire gene expression system. These models incorporate the processes of photoactivation, deactivation, thermal reversion, and the dynamic behavior of the light-activated gene promoter system. For meticulous control of the system, we determined the rate constants of the integrated stochastic model using an omniscient deep neural network. This network is capable of mapping the combinations of rate constants directly to time-dependent joint state distributions. By modulating activation rates through alterations in light intensity and adjusting degradation rates via N-terminal mutagenesis, we demonstrate that the optically-controlled perturbations can precisely modulate molecular noise. Our findings highlight the potential of employing an optically-controlled gene perturbation system as a noise-managed stimulus source. Furthermore, they suggest the feasibility of inferring rate constants by monitoring system behavior, facilitated by the predictive capabilities of the deep neural network.

Results

Perturbing gene expression dynamics with light

In order to achieve high spatial-temporal precision in tuning gene expression, coupled with quantitative control, we have designed an optically-controlled perturbation system. This system is based on the light-sensitive Phytochrome B (PhyB) from *Arabidopsis thaliana*, drawing inspiration from the work of Shimizu-Sato et al.⁴¹. The full-length PhyB photosensory module (PSM) is comprised of four domains: the N-terminal extension (NTE), the Period/ARNT/Single-minded (PAS) domain (nPAS), the cyclic GMP-regulated cyclic nucleotide phosphodiesterase/Adenylate cyclase/FhlA (GAF) domain that binds the tetrapyrrole chromophore (PΦB), and the phytochrome-specific domain (PHY). At the interface between nPAS and GAF, there exists an intricate figure-eight knot, referred to as the “light-sensing knot,” which is intimately associated with the chromophore and plays a critical role in signal transduction. The PSM’s structure is reinforced by a light-sensing knot loop (KL) and a hairpin (HP), which interconnect the NTE, GAF, and PHY domains. In our study, we utilized only the N-terminal fragment (residues 1-621) of PhyB, encompassing the essential photosensory module (PSM) while lacking the dimerization/nuclear import module (DNM; also known as the output module in its prokaryotic counterparts), which facilitates dimerization and nuclear translocation of the Pfr form⁴². In contrast to the full-length PhyB *in planta*, the PhyB N-terminal (PhyB(NT)) is monomeric *in vitro*, devoid of the DNM^{43,44}. For the construction of a light-sensitive, switchable molecular system, we selected PIF3 as the binding partner for PhyB(NT). PIF3 comprises three domains: the Active Phytochrome B-binding (APB) motif, the Active phytochrome A-binding (APA) motif, and the basic helix-loop-helix (bHLH) transcription factors. The APB motif preferentially interacts with the light-sensing knot within the N-terminal photosensory module of photoactivated PhyB. While PIF3 is capable of forming homodimers via its bHLH domain in its full-length state⁴⁵, its interaction with monomeric PhyB(NT) promotes a monomeric state in PIF3.

For the additional components of the optically-controlled perturbation system, instead of employing the Gal4 DNA-binding domain (Gal4-DBD) and the Gal4 activation domain (Gal4-AD) fusions for the functional modules, we utilized the LexA DNA-binding domain (LexADBD) and the VP16 activation domain (VP16AD). These combinations are commonly employed in yeast two-hybrid assays. We engineered two fusion proteins, LexADBD-PhyB(NT) and PIF3-VP16AD, to regulate gene expression via light induction. Both components were integrated into the yeast genome and expressed under the control of the constitutive promoter *PADHI*. After translation, LexADBD-PhyB(NT) is synthesized in the inactive Pr state and preferentially accumulates in the cytosol in the absence of light. Consequently, in dark conditions, the photoreceptor accumulates in this inactive state, ready to be activated upon light exposure. For the reporter gene construction, LexA binding sites

were fused to a segment of the *GALI* promoter encompassing the TATA box. Thus, the PhyB(NT)/PIF3 interaction modulates expression from a synthetic promoter comprising four LexA binding sequences, with each sequence capable of binding two LexA molecules. Upon light activation, the PSM domain of PhyB(NT) undergoes a conformational change and binds to PIF3-VP16AD. This interaction facilitates the binding of VP16AD to the TATA box, triggering the expression of a fluorescent reporter for observation. The degree of photoconversion from Pr to Pfr correlates directly with the number of red photons administered, which is expected to provide precise dosage control in a highly predictable and reproducible manner⁴⁶. Light also enables high spatial-temporal precision in control. Such precise regulation of gene expression is crucial for perturbing cell state dynamics. To modulate the stability of the fluorescent reporter protein for rapid degradation and enhanced signal sensitivity, we employed a ubiquitin fusion technique. This method allows for the alteration of protein degradation rates by revealing a destabilizing residue following the co-translational removal of ubiquitin⁴⁷. A schematic representation of the optically-controlled gene expression system is depicted in Fig. 1(A).

The optically-controlled system is expected to respond rapidly in the presence of red light and to be deactivated by far-red light⁴⁸. Owing to the low basal transcription rate, minimal activation is anticipated in the absence of light⁴¹. We monitored the dynamics of reporter expression using a microfluidic chip designed for the long-term incubation of thousands of cells (see Methods for a detailed description of the microfluidic chip fabrication). A representative experimental result is depicted in Fig. 1 (B). We observed that pulsed light activation induces sustained protein expression, as illustrated in Fig. 1 (C). This behavior contrasts with the blue light-regulated gene expression system, which demonstrated consistent protein expression under continuous light activation and rapid deactivation in the absence of light^{40,49}. Moreover, this system exhibits significant fluctuations in gene expression compared to chemically induced gene expression systems. These observations suggest that protein expression in our system can be finely tuned by modulating the reaction rates of the light-responsive components and that the underlying mechanisms of light response in our optical perturbation system are fundamentally different from those in the blue light-regulated gene expression system. Prompted by these findings, we proceeded to investigate the photoconversion and thermal reversion processes of PhyB in the presence of PIFs.

Modeling the photoconversion and thermal reversion process of phytochromes

Most land plants, particularly *Arabidopsis*, possess several phytochromes, which are prevalent in angiosperms and can be categorized into three primary types: Phytochrome A (PhyA), PhyB, and PhyC⁵⁰. These phytochromes are bilin-binding photosensory receptors that undergo light-induced conformational changes. These changes facilitate interactions with signaling partners, especially transcription factors or the proteins that reg-

ulate them, leading to extensive transcriptional reprogramming. Consequently, phytochromes orchestrate a variety of physiological processes, including seed germination, chloroplast development, seedling de-etiolation, shade avoidance, photoperiodic regulation of flowering time, and ultimately, senescence⁵¹. Among these types, PhyA and PhyB have similar absorption spectra, yet they exhibit significant differences in their action spectra for physiological responses. PhyB is primarily active under red light, while PhyA functions effectively under far-red light, where PhyB's activity is suppressed. This dichotomy has spurred extensive research into their distinct roles.

In the case of PhyB, bilin phytochromobilin (PΦB) serves as the chromophore, absorbing energy from red light and transferring it to the protein's structure. During the photoconversion process, light-induced bilin isomerization prompts a conformational rearrangement, converting the dark-adapted, biologically inactive Pr state into a metastable, far-red light-absorbing Pfr state, which is biologically active. The partial overlap of their absorption spectra leads to a dynamic photo-equilibrium between the Pfr and Pr forms, which varies with the light wavelength. Pfr is produced exclusively through photoconversion and can revert to the Pr form either through the absorption of far-red light or via spontaneous relaxation—a temperature-dependent, non-photochemical process known as thermal reversion. Thus, the interplay between photoconversion and dark reversion dictates the steady-state levels of the active Pfr conformation, enabling the dynamic sensing of light quality and quantity. Consequently, signal transduction is modulated by a combination of light intensity, wavelength, and temperature, in accordance with plant requirements⁵². Upon exposure to inductive wavelengths, PhyB adopts a functional dimeric conformation, enabling photosensitive responses and resulting in three potential phytochrome species: Pr-Pr, Pfr-Pr, and Pfr-Pfr^{42,44,53}. The intracellular protein dynamics among these PhyB dimer species dictate their activity potential, with only the nuclear Pfr-Pfr homodimer initiating PhyB responses⁴⁴.

Analysis of *in vitro* photoconversion induced by red light in *Arabidopsis* revealed a monomeric process following single-exponential kinetics⁵⁴. In contrast, the Pfr to Pr photoconversion under far-red light illumination is more accurately described by a bi-exponential kinetic fit. Additionally, at room temperature (22°C), total Pfr reverted entirely to the inactive form (Pr) following bi-exponential decay kinetics in darkness^{43,54}. The bi-exponential kinetics observed in both photoconversion and thermal reversion may result from sequential reactions, the presence of multiple conformers, or a combination of these scenarios. Previous studies have identified intermediates of phytochromes on the millisecond timescale^{55,56}, yet no intermediates have been detected on the timescale of hours during the thermal reversion of phytochromes. Consequently, we propose that the bi-exponential decay arises from two distinct forms of Pfr within the molecular population^{42,43,52,57–60}. On the other hand, thermal reversion is also modulated by protein interactions. The Pfr-Pfr homodimers exhibit greater

stability than the Pfr-Pr heterodimers; the additional subunit interactions in Pfr-Pfr homodimers confer a stabilization of approximately 4 kcal/mol⁶¹. Photoconversion of only one subunit in the phytochrome dimer from Pr to the metastable Pfr conformation could lead to a reduced stability of the Pfr-Pr heterodimer, thereby favoring a light-independent back reaction to the Pr-Pr homodimer. This phenomenon results in a more pronounced decline of PhyB responses at longer wavelengths. The rate of thermal reversion for the Pfr-Pr heterodimer is approximately 100-fold faster than that of the active Pfr-Pfr homodimer, enabling PhyB to perceive temperature fluctuations both diurnally and nocturnally⁴⁴. Studies of *Arabidopsis* PhyB expressed in yeast have revealed that the dark reversion rates of Pfr-Pfr homodimers are an order of magnitude lower than those of Pfr-Pr heterodimers⁶¹. The interaction of PhyB with ARR4 (*Arabidopsis* Response Regulator 4) diminishes the dark reversion of the Pfr conformer, thus modulating light sensitivity in *Arabidopsis*⁶². Furthermore, phytochromes demonstrate prolonged persistence of the Pfr state when associated with nuclear bodies (NBs), attributable to the suppression of thermal reversion in darkness⁴⁴. The binding of PhyB(NT) to PIF can also inhibit the thermal reversion process^{43,52}. Collectively, these findings suggest that the photoconversion rate of phytochrome from Pfr to Pr is contingent upon the wavelength and fluence rate of light, while the thermal reversion rate is influenced by temperature and the presence of binding partners.

To consolidate the findings of prior studies, we introduce a streamlined model to encapsulate the photoconversion and thermal reversion mechanisms of phytochromes, as depicted in Fig. 2 (A). This model is akin to the dual-pathway framework suggested by⁶³. It posits the existence of two photo-activated conformers, Pfr₁ and Pfr₂, inferred from the bi-exponential kinetics characteristic of the thermal reversion process⁵⁴. The model allows for the PIF binding partner to interact with both the Pfr and Pr states, with the latter also capable of basal affinity binding to Pa⁶⁴. Photoconversions are postulated to occur in the dimeric state, with rate constants mirroring those of the monomeric state. To determine these rate constants, we devised a score-based bootstrap inference algorithm that leverages *in vitro* equilibrium data from photoconversion and thermal reversion assays, as illustrated in Fig. 2 (B, C). The score is defined by the equation

$$S = \sum_t \int \|\mathbf{x}(t) - \mathbf{y}(t)\|_2 d[\mathbf{x}(t)], \quad (1)$$

representing the mean L2-norm discrepancy between the model's theoretical predictions and the empirical data across all observable time points. For each set of experimental conditions, we compute the score using 10 simulated trajectories, each generated with the Gillespie exact kinetic sampling algorithm³⁷. The inference algorithm iteratively adjusts the rate constants to minimize the score via the steepest descent approach. The photoconversion rates are influenced by the light's wavelength and fluence rate; red light catalyzes both the Pr

→ Pfr and Pfr → Pr transitions in phytochromes. For the sake of simplicity, we characterize photoconversion using effective rates corresponding to specific light wavelengths. That is, when modeling the Pr → Pfr (Pfr → Pr) photoconversion, the rate for the Pfr → Pr (Pr → Pfr) transition is set to zero. Additionally, while *Arabidopsis* PhyB(NT) exhibits single-exponential kinetics under red light, we assign different photoconversion rates to Pr → Pfr₁ and Pr → Pfr₂ to achieve a more accurate model, as evidenced by a reduced score.

The chemical reactions and rate constants inferred are detailed in the SI Appendix, Table S2. The photoconversion of Pfr₁ → Pr occurs approximately 3-fold faster than that of Pfr₂ → Pr, while the thermal reversion of Pfr₂ → Pr is roughly two orders of magnitude slower than that of Pfr₁ → Pr. Consequently, the Pfr₂ state is a photo-activated state that forms slowly but exhibits greater stability compared to Pfr₁. Upon binding to PIFs, the thermal reversion rate is reduced by an order of magnitude for both Pfr₁ → Pr and Pfr₂ → Pr, with the reversion of Pfr₂ → Pr remaining two orders of magnitude slower than that of Pfr₁ → Pr. The dissociation constants K_D for Pfr₁Pa and Pfr₂Pa are 0.56 and 23.81, respectively, signifying that Pfr₁ has a stronger affinity for PIFs than Pfr₂. For PrPa, $K_d = 6.23 \times 10^4$, which is approximately four orders of magnitude greater than that for Pfr₁ and two orders of magnitude greater than that for Pfr₂, aligning with the findings of previous studies⁶⁴. Our analysis suggests a model with two photo-activated conformers that can account for the observed photoconversion and thermal reversion behaviors of phytochromes both in isolation and when associated with PIFs. The photoconversion rates of Pr → Pfr₁ and Pr → Pfr₂ are comparable. However, Pfr₂ demonstrates enhanced stability in terms of both photoconversion and thermal reversion. The binding of PIFs further stabilizes the photo-activated state, leading to a reduced rate of deactivation that mirrors the behavior observed *in planta*^{42,44,61,62,65,66}. As depicted in Fig. 2 (C), our findings surpass those of the prior study by Smith et al., which did not accurately predict the thermal reversion process at elevated PIF concentrations⁴³. Moreover, our model presupposes the existence of only two activated conformers, obviating the need to postulate a secondary activated state for phytochromes. Collectively, these results affirm that our model effectively captures the comprehensive behavior of photoconversion and thermal reversion processes in phytochromes, both independently and in the presence of PIFs. We have therefore employed the framework of this streamlined model to analyze the optically controlled gene expression system.

Stochastic modeling and parameter screening with omniscient neural network

We monitor the real-time kinetic signal to conclude that the system has a distinct dynamical behavior compared to those systems activated by blue light^{40,49}. In the blue light-activated systems, the light-switchable promoter gradually ceases to produce protein upon light removal. However, our system behaves differently: it is activated and remains active until exposed to deactivating light. The light filtering pattern in the blue light-

activated systems can originate from its light-out dissociation (LOD) behavior. In contrast to these systems, where the memory of the expression state is gradually lost in darkness, the dimeric dynamics of PhyB lock the system in the activated state, leading to a robust memory effect. Considering both strong and weak memory, and the confidence in these two mechanisms, the biophysical properties of our system endow it with unique signaling capabilities: a strong memory signaling with an enhanced transfer function.

Given the highly stochastic fluorescent signals from the gene expression trajectories controlled by PhyB-based optical regulators (Fig. 1 (C)), a deterministic description of the system is precluded^{34,35}. Therefore, from the perspective of probabilistic modeling, we represent the optically-controlled gene expression regulated by phytochromes as a non-Markovian stochastic dynamical system that is responsive to external controls. A stochastic reaction network has been constructed for this system⁶⁷. In light of the evidence presented in the previous section, which reveals two activated conformers through fitting to photoconversion and thermal reversion processes, we have modeled the system comprising 23 species and 74 reactions, as depicted in Figure 3(A) and listed in Table S3.

The control of gene expression by light, as described in the previous section, involves altering light exposure to red or far-red light, which modulates the rate constants of photoconversions and can initiate or terminate mRNA transcription. The activation function of the promoter is modeled as a step function, aligning with the timescale separation where PhyB-PIF3 binding occurs within milliseconds, and gene transcription takes place over seconds. To address the fluorescent background issue associated with the basal expression of the fluorescent reporter, we initiate the modeling 12 hours prior to the experimental start time. The complete control protocol is as follows: 12+2 hours of dark incubation, a 2-minute red-light pulse for activation, a subsequent 5-hour dark incubation, and finally an 8-hour deactivation period under far-red light. The system then reaches a NESS prior to the experiment, reflecting the actual system setup. The background cellular fluorescence signal intensity is then used to calibrate the steady-state distribution of the fluorescent reporter generated by basal expression. Consequently, the distribution of the background signal also provides insights into the rates of basal transcription and degradation. Furthermore, calibrating the background signal determines the ratio factor R for converting fluorescent intensities to the number of molecules, defined by the equation:

$$R = \frac{\text{Fluorescent intensity (a.u.)}}{\text{Number of reporter molecules}}$$

where R is expressed in arbitrary units (AU). During the experimental time frame, the ratio factor is assumed to remain constant, independent of the number of reporter molecules present. Hence, for each experiment, a consistent ratio factor is applied to accurately fit the stochastic model to the experimental data.

For extended two-state stochastic gene expression systems, distributions can be analytically obtained³³. However, solving the PhyB-based optically-controlled gene expression system analytically is infeasible due to its large state space. Numerical methods, such as kinetic Monte Carlo methods³⁷, can be employed to approximate the joint state probability distribution. Yet, sampling from the posterior distribution given a general prior and experimental data remains impractical with these methods because of the prohibitive computational time. For example, estimating the likelihood requires simulating approximately 10^4 trajectories for each set of rate constants. Typically, for a single set of rate constants, each estimation takes about 10 minutes using a parallel algorithm. To accurately estimate the posterior distribution, it is necessary to sample 10^4 combinations of rate constants, not including the potentially more numerous mixing steps. Consequently, even with a reasonably informative prior, one inference can take an estimated 60 days to complete, rendering the process highly inefficient. This limitation is analogous to other numerical methods, such as finite state projection approaches, which track the joint state probability distribution within a truncated state space⁶⁸.

To surmount this obstacle, we employ a neural network strategy to estimate the time-dependent state distribution using variational approximations. The neural network’s architecture is depicted in the SI Appendix, Fig. S2. The inputs to this network consist of prompts, which include the rate constants $\boldsymbol{\sigma}$, the initial condition \mathbf{x}_0 , and the time value $t - t_0$, as well as the state vector at the current time \mathbf{x}_t . The network’s outputs are the conditional marginal probabilities of the state coordinates given the prompts’ information, denoted as $\hat{p}^\theta(x_t^{(i)} | x_t^{(1)}, \dots, x_t^{(i-1)}, \boldsymbol{\sigma}, \mathbf{x}_0, t - t_0)$. The conditional joint probability of the state is thus expressed as

$$\hat{p}^\theta(\mathbf{x}_t | \boldsymbol{\sigma}, \mathbf{x}_0, t - t_0) = \prod_{i=1}^N \hat{p}^\theta(x_t^{(i)} | x_t^{(1)}, \dots, x_t^{(i-1)}, \boldsymbol{\sigma}, \mathbf{x}_0, t - t_0)$$

To delineate the mapping from the amalgamation of prompts and states to the conditional marginal probabilities, we implement a masked multi-head self-attention block that computes the scaled dot-product attentions. The outputs from the multi-layer decoder, composed of masked multi-head attention blocks, are subsequently fed into a language model head. This head is designed to project the decoder outputs onto probability weights, which are then normalized using the softmax function (see Methods for more details).

To demonstrate the accuracy and efficiency of the neural network approach, we trained a neural network on a dataset comprising 256 trajectory ensembles, each consisting of 1,000 trajectories corresponding to a unique combination of rate constants. The trained neural network subsequently provided the conditional likelihood $\hat{p}^\theta(\mathbf{x}_t | \boldsymbol{\sigma}, \mathbf{x}_0, t - t_0)$, facilitating parameter screening. As illustrated in Fig. 3 (B), despite the neural network being trained on only 256 trajectory ensembles, the means and standard deviations of states generated from the neural network’s predictions for 2,400 prompts closely mirror those obtained from stochastic simulations. Owing

to the highly parallel computation capabilities of the neural network on General-Purpose Graphics Processing Units (GPGPUs), the computation of the joint state probabilities for 2,400 prompts can be completed within one hour. This represents a significant improvement in efficiency compared to traditional methods, which typically require approximately 40 hours for similar computations.

Inferencing the rate constants with neural network assisted Monte Carlo sampling

Estimating the likelihood using a trained neural network provides a unified framework for inferring rate constants from a dataset that includes both time-slice and kinetic data (see Methods for more details). This approach allows for the integration of information derived from multiple measurement techniques, encompassing both time-slice and real-time kinetics of any species, to enhance the accuracy of inference. In contrast, the previous non-parametric Bayesian method utilized only time-slice data for a limited number of species³⁸. For systems with many species, solving the chemical master equation is computationally formidable, and representing the state distribution is also memory prohibitive. Nevertheless, our neural network-based method is not constrained by these limitations (unpublished data).

Given the constraints of computational resources, we have approximated certain rate constants using values sourced from prior researches. The basal transcription rate of the reporter gene, absence from any regulatory binding, was established at 0.001 min^{-1} . This rate negligibly impacts the basal reporter distribution. Transcription rates for PhyB and PIF were inferred from the nascent transcription rates of yeast genes, as reported in^{69,70}, which vary between 2 and 30 hour^{-1} . Adopting the upper limit of this range, 0.5 min^{-1} , we approximated the transcription rates of PhyB and PIF to be 0.31 min^{-1} and 0.33 min^{-1} , respectively. We postulate identical activated transcription rates for the reporter gene when bound to Pfr₁Pa, Pfr₂Pa, and PrPa. Translation rates for PhyB, PIF, and the reporter were estimated from translation initiation and elongation rates derived from ribosome profiling data⁷¹, with the translational rate constant ranging between 5 and $8 \text{ residues sec}^{-1}$. By applying the highest observed rate, we estimated the translation rates for PhyB(NT)-lexDBD, PIF3-VP16, and the reporter inclusive of a ubiquitin fragment to be 9.573 min^{-1} , 0.775 min^{-1} , and 1.89 min^{-1} , respectively. Post-translation, proteins must properly fold to become functional. The median folding time, $t_{50} = 0.005 \text{ sec}$, as sourced from a protein database and adjusted for temperature, equates to a rate constant of 8317.8 min^{-1} is used for both PhyB(NT)-lexDBD and PIF3-VP16⁷². The maturation time for the reporter (sfGFP), $t_{50} = 6.9 \text{ min}$, was derived from *in vivo* studies of fluorescent protein maturation in yeast cells, corresponding to a rate constant of 0.1 min^{-1} ⁷³. We have assumed uniform mRNA degradation rates for PhyB, PIF, and the reporter. Additionally, we posit that the degradation rates for both immature and mature proteins are equivalent.

Four rate constants were identified as having the most significant effects on the behavior of the system. The

first is the activated transcription rate of the reporter (σ_{PR}), which largely determines the steady-state distribution of the number of molecules. Another is the association rate of Pr with Pa (α_{PrPa}), which greatly influences the basal expression level. Finally, the degradation rates of mRNAs (β_{mRNA}) and the reporter (β_{PR}) define the steady-state distribution after deactivation. Using the trained neural network model, we drew samples from the posterior distribution of the rate constants using a Markov Chain Monte Carlo method (see Methods for details). As shown in Fig. 3 (C), the four rate constants, σ_{PR} , α_{PrPa} , β_{mRNA} , and β_{PR} , are tightly constrained by the experimental data. Utilizing the most probable values of these rate constants for inference, we performed a stochastic simulation of the system and compared the predicted state distribution with the experimental histogram, as depicted in Fig. 3 (D). The complete plots across 48 time points are presented in the SI Appendix, Fig. S5. It is evident that the inferred rate constants accurately capture the state distribution of the fluorescent reporter. The complete list of rate constants is provided in the SI Appendix, Table S3.

Modulation of gene expression noise by light

For the purpose of applying our optical perturbation system to the study of cellular noise in biological systems, it is essential to be predictive for the output noise of our system. Thus, we investigated the possibility of precise noise control by employing variable light intensities and modulation of the degradation rate of the target molecule. To tune the exposure light intensities, we calibrated the light source of the microscope and applied a linear increase in light intensities to activate the system. Additionally, we modulated the degradation rate of the reporter protein by expressing a chimeric ubiquitin-X-reporter construct. Upon expression, ubiquitin is co-translationally removed from the protein, leaving behind the X-reporter, where X represents the chosen amino acid residue. The N-terminal residue of a protein significantly influences its half-life, which can vary from several hours (as in the case of methionine or alanine) to a few minutes (for residues like leucine or arginine)^{74,75}. Subsequently, we evaluated the behavior of our system under conditions of linearly increasing light intensities and following N-terminal mutagenesis.

As shown in Fig. 4 (A, B), the steady-state distributions of the reporter indicate changes in the rate constants due to varying light intensities and N-terminal mutagenesis. We further sought the optimal rate constants for photoconversions as well as degradation using a score-based bootstrap inference algorithm (Eq. 1). The comparisons between the molecular number distributions predicted by the inferred rate constants and the experimental histograms is presented in the SI Appendix, Figs. S3–S7. The Hellinger distances between the predicted distributions and the experimental results are around 0.1, which attests to the efficacy of the inference algorithm. From Fig. 4 (C), it is observed that within the range of 20%–60% light intensities, there is an almost linear increase in the rate constant for the reaction $Pr \rightarrow Pfr_2$. In contrast, the rate constant for the reaction

$\text{Pr} \rightarrow \text{Pfr}_1$ increases exponentially. Consequently, the extent of photoconversion from Pr state to Pfr states is directly correlated to the quantity of red photons provided, exhibiting high predictability and reproducibility. However, both rate constants diminish to minimal values when the light intensity reaches 80%, likely due to phototoxicity at high light fluences⁴¹.

To quantify the change in cellular noise during the modulation of rate constants, we calculated the logarithm of the coefficient of variation (CV), defined as $\log_{10}(\sigma/\mu)$, where σ represents the standard deviation and μ denotes the mean number of molecules. As depicted in Fig. 4 (D), the logarithm of the CV decreases with an increase in activation rates and increases with the degradation rate. The dependence of the logarithm of the CV on the rate constant of $\text{Pr} \rightarrow \text{Pfr}_2$ is linear, whereas its dependence on the input light intensities is predominantly exponential. The slight deviations from linear and exponential dependencies suggest that the $\text{Pr} \rightarrow \text{Pfr}_2$ transition contributes significantly to the noise behavior of the system. Furthermore, an exponential dependence on light intensities implies that the noise intensity has an intrinsic lower bound in the PhyB-based optical perturbation system. Conversely, the noise's dependence on the degradation rate constant is exponential, indicating that the degradation rate constant's influence on noise is pronounced when its value is small.

The complex behavior of the system can be comprehensively understood through the lens of the so-called inverse correlation between noise and mean expression level, as illustrated in the SI Appendix Fig. S8. Both activation and deactivation in the optically-controlled perturbation system modulate the expression level and the expression noise simultaneously, with the noise being linearly dependent on the mean population of molecules. This relationship between noise and mean population level has also been observed for both protein and mRNA in numerous other systems⁷⁶⁻⁷⁹. However, the PhyB-PIF3 system exhibits a high level of noise relative to its mean expression level compared to other light-modulation systems⁷⁶. Considering the dual-pathway mechanism of the PhyB system, it is conceivable that an increase in transition pathways maintains the linear dependency relationship while elevating the ratio of this linear dependency between noise and the mean population level of molecules.

Discussion and conclusion

Understanding the behavior of noise in biological systems is crucial for comprehensively characterizing the phenotypic changes in many key processes, including gene expression, signal transduction, development, and evolution. While numerous single-molecule labeling methods are available and high spatial-temporal resolution can be achieved through optogenetic techniques, quantitatively describing noise remains a significant challenge. Two major obstacles are the modeling of complex biochemical reactions and the inference of rate constants for

these models, both of which have garnered considerable attention.

In this work, we present a systematic approach to elucidate the dynamic behavior of cellular noise using our optical perturbation system combined with deep learning. We demonstrate that the optically-controllable system we have developed constitutes a highly sensitive light modulation system. It exhibits distinct behaviors compared to the blue light-regulated gene expression system^{40,49}. The dynamic mechanism of the blue light-regulated system can be characterized by Hill functions, whereas our PhyB-based system is more accurately described by a multiple-path reaction system involving two activated conformers. Moreover, the blue light-regulated system has a faster thermal reversion rate compared to the PhyB-based system. Activation by blue light of these systems leads to a gradual deactivation in these systems, resulting in a decreased population of the activated state. However, the stability of the activated Pfr states of phytochromes is significantly enhanced in the presence of PIFs. As the result, the PhyB-based system not only retains memory for long time duration but also allows for the accumulation of light fluence over prolonged periods. This characteristic renders it a highly stable two-state light-regulated gene regulator when compared with the blue light system. Both pulsatile and continuous activation modes can be achieved through the interplay of red and far-red light, without the need for continuous light illumination. This endows the PhyB-based system with advantages in *in vivo* applications, such as the semi-automatic control of glucose homeostasis or immunotherapy by epigenetically engineered photosensitive cells^{14,80}.

To further quantitatively characterize the dynamical properties of our system, we developed a stochastic model comprising 74 reactions. To infer the rate constants of this model, we introduced an omniscient neural network capable of mapping the rate constants directly onto joint state distributions. The trained network facilitates efficient computation of likelihoods for various rate constant configurations. We demonstrate that rate constants can be determined with high efficiency and precision using the omniscient neural network, surpassing conventional methodologies. Comparing the stochastic model's predictions with experimental data, we show that our system can not only produce a controllable level of target molecules but also modulate expression noise through adjustments in light intensity and the degradation rate of the target protein.

In conclusion, we showcase a novel integration of optical perturbation with a neural network-based likelihood estimator to dissect noise in biological systems. Our methodology is readily extendable to diverse optogenetic systems and organisms, enhancing the elucidation of complex dynamical behaviors in state distributions for expansive systems.

Material and methods

Strains and plasmids construction

All experiments were carried out in W303a (*MATa leu2-3,112 trp1-1 can1-100 ura3-1 ade2-1 his3-11,15*), a haploid derivative of W303 obtained from ATCC (#208352). Plasmids were constructed and propagated in *E. coli* DH5 α and verified via Sanger sequencing prior to strain construction. Standard protocols for the growth, maintenance, and transformation of yeast and bacteria, as well as DNA manipulation, were employed. Initial plasmids were assembled as described in a previous study⁴¹, with functional fragments cloned from cDNA by conventional PCR. DNA digestion and ligation utilized restriction endonucleases and T4 DNA ligase from New England Biolabs (USA). Light-responsive strains were generated by integrating pAM206 into the *trp1* locus of the W303a yeast genome. Given that pAM206 harbors two XbaI sites, partial digestions were executed using the XbaI endonuclease to optimize the yield of linearized plasmids. These linearized plasmids were subsequently transformed into yeast cells following the standard lithium acetate-based transformation protocol. Transformed cells were cultured on selective auxotrophic minimal media using the appropriate dropout plates (Takara). Integration of plasmids was confirmed by genomic PCR at both the N- and C-terminal sides of the recombination loci. In light of the fact that multiple copies can lead to high expression levels and considerable expression noise, potentially complicating expression kinetics⁷⁶, single-copy integration was verified using real-time quantitative PCR. The resultant strains expressed PhyB(NT)-lexADBBD. Subsequently, pAM205 was linearized with ClaI and integrated into the *leu2* locus, resulting in strains that additionally expressed PIF3-VP16AD. The strain produced through sequential integration served as the progenitor for all subsequent experiments. To modify the stability of the reporter, pAM236M was engineered by appending an ubiquitin sequence upstream of the fluorescent protein in pAM236. The N-terminal methionine (M) of pAM236M was altered to arginine (R) through site-directed mutagenesis, thereby modulating the stability of the reporter via the N-end rule pathway⁷⁴. To replace the fluorescent reporter Venus with sfGFP, which offers enhanced photostability and accelerated maturation⁸¹, the sfGFP sequence was initially PCR-amplified from the GTTg plasmid (Addgene #81109) and subsequently fused with the backbone sequences of pAM234 and pAM236 via inverse PCR. Comprehensive plasmid information is available in Table S1. The functionality of the final constructs was confirmed by fluorescence microscopy following co-incubation with PCB. Control assays were conducted using PhyB-only and PIF3-only cell strains under identical conditions for validation.

Fabrication of microfluidic chip for real-time kinetic measurements

The design and fabrication of the microfluidic device for live-cell imaging adhered to protocols from previously published work⁸². Briefly, the process utilized SU-8 2000 series photoresists (MicroChem), chrome glass masks (HTA Photomask), and an EVG620 contact mask aligner (EV Group) to construct and pattern the desired features on silicon wafers supplied by University Wafer Inc. The feature heights were confirmed with a Dektak 150 surface profiler (Veeco). Each chip comprised four identical microfluidic devices, each inspected meticulously to ensure the absence of dust or defects. Prior to cell introduction, the microfluidic chip was cleansed with acetone and isopropanol, followed by at least two rinses with sterilized deionized water to remove any residual solvents. The chip was then positioned on a custom gas chamber situated on the stage of an inverted microscope. This setup was enclosed within a thermally stable microscope cage incubator (Okolab), maintaining a constant temperature of 30 °C. The media ports were connected to plastic tubing, which in turn was linked to a high-precision pump supplying fresh media. The waste port of the chip was attached to plastic tubing leading to a 50 mL collection tube.

Media and growth conditions

Cells were initially cultured in synthetic complete (SC) medium (pH 6.0) overnight until the optical density at 600 nm (OD_{600}) reached approximately 1.0, prior to initiating experiments. For cell loading, the yeast culture was transferred using a syringe, driven by a pump at a flow rate of 0.1 mL/min. The majority of the traps were populated with cells within 1-2 minutes. Subsequently, the medium in the syringe was replaced with SC medium supplemented with 25 μ M of PCB, and the cells were incubated for a minimum of 2 hours in the absence of light. For the light-activated kinetic assays, the flow rate of the medium was set to 0.01 mL/min to minimize cell movement and maintain a normal growth rate.

Light activation procedure and measurements

The structural analogs of phytochromobilin (P Φ B), phycocyanobilin (PCB) (CAS No. : 20298-86-6), are utilized to induce the photoconversion of PhyB. We employed a Semrock 641/75 nm bandpass filter and a Semrock 715 nm long-pass filter for light activation and repression, respectively. For light activation, red light at 20%, 40%, 60%, and 80% constant intensities was applied for 2-minute intervals to initiate gene expression. Conversely, for light repression, far-red light at a constant 50% intensity was used to effectively suppress transcription in the light-regulated system. Fluorescent reporter activity was monitored using 488 nm laser illumination with an exposure time of 100 ms.

Image analysis with point-prompt cell segmentation

To analyze the microscopic images, we have developed a Python-based software that facilitates efficient cell segmentation and cell tracking. The software employs the Segment Anything Model (SAM) as its core model, which is capable of segmenting yeast cells using point-prompt information⁸³. Following the SAM-based segmentation, the masks of the segmented cells are manually refined through interactive labeling. Subsequent to segmentation, cell labels are reassigned using automatic tracking via the Hungarian algorithm. The automatically segmented and tracked cells are subsequently manually reviewed to correct any mislabeling and to exclude dead cells. Finally, each cell’s fluorescence intensity, as well as morphological information, are collated and exported to a text file for additional analysis.

Simulation of stochastic reaction network

To account for the basal expression of reporter proteins, we simulated the entire process from -12 hours until the initiation of the experiment. Red light activation was applied at 840 minutes for 2 minutes, and the system was deactivated using far-red light at 1142 minutes until the conclusion of the experiment. The total duration of the simulation was 1624 minutes. We utilized the `biocircuits` package for parallel simulations employing the Gillespie algorithm. For each set of rate constants, $10^3 - 10^4$ trajectories were generated, and system states were recorded at time points corresponding to the experimental sampling times. To initially train the autoregressive model in a supervised manner, we simulated trajectory ensembles for 256 sets of rate constants, where the rate constants were sampled using the quasi-Monte Carlo method with the Sobol sequence.

Architecture of the omniscient neural network model

For modeling the light-regulated gene expression system, we have used the variational approach to approximate the joint distribution of states given prompts that encode information of rate constants and time. We designed the omniscient neural network model with masked multi-head self-attention blocks as its core functional module which describes the connection between prompts and states. For calculating the self-attention score, we use learnable embeddings to convert the state vector $\mathbf{x} \in \mathbb{R}^N$ to a tensor in the embedding space $X \in \mathbb{R}^{N \times d_{emb}}$. On the other hand, we collect the logarithm of rate parameters and time value in sequence to construct the prompt. To handle the continuous variables of rate parameters and times in the prompt, we first transform rate parameters into logarithmic values to reduce value divergences. Then, we employ a one-layer perceptron to project the prompt to a vector \mathbf{p} with fixed length d_p . We then map \mathbf{p} to the same embedding space as the discrete-valued states with linear projector, to obtain the tensor $Y \in \mathbb{R}^{d_p \times d_{emb}}$. The concatenation

of X and Y serves as the input tensor $Z = \text{Concat}(X, Y) \in \mathbb{R}^{d_s \times d_{emb}}$ to the network, where $d_s = N + d_p$. The masked multi-head self-attention block calculates the scaled dot-product attention of the input tensor Z with h attention heads

$$\text{Attention}(Z) = \text{Concat}(\text{head}_1, \dots, \text{head}_h)W_O$$

$$\text{where } \text{head}_i = \text{Softmax}\left(\frac{\text{Mask}(Q_i K_i^T)}{\sqrt{d_k}}\right) V_i$$

where the query $Q_i = ZW_{i,Q} \in \mathbb{R}^{d_s \times d_k}$, the key $K_i = ZW_{i,K} \in \mathbb{R}^{d_s \times d_k}$, and the value $V = ZW_{i,V} \in \mathbb{R}^{d_s \times d_v}$ are all linear projections of the input tensor Z . These projections are obtained using different learnable parameter matrices: $W_{i,Q} \in \mathbb{R}^{d_{emb} \times d_k}$, $W_{i,K} \in \mathbb{R}^{d_{emb} \times d_k}$, $W_{i,V} \in \mathbb{R}^{d_{emb} \times d_v}$, and $W_O \in \mathbb{R}^{hd_v \times d_{emb}}$. Here, d_k and d_v represent the dimensions of the number of query (key) elements and value elements for each state value, respectively. When h is specified, d_k and d_v are defined according to the relation $d_k = d_v = d_{emb}/h$. The attention mask $\text{Mask}(\cdot)$ is used to conceal the dependency relations between the previous position and subsequent positions of both the prompt and the generated sample states. This is achieved by assigning $(Q_i K_i^T)_{\xi < \mu} = -\infty$, where ξ and μ are the row and column indexes of the $Q_i K_i^T$ matrix, respectively. We stack multiple attention blocks to create a multi-layer decoder, which enhances network's representational capability. The output of the masked multi-head attention block $A \in \mathbb{R}^{d_s \times d_{emb}}$ is used as the input for another block. Following the multi-layer decoder, a language model head is utilized to map the decoder outputs to probability weights, which are then normalized using the softmax function. The predictions of the MET provide joint distributions of states given the input prompts.

Coordinate embedding and training of the omniscient neural network model

The synthesis of mRNA and the expression of proteins are significantly influenced by the biochemical rates associated with each reaction. The number of protein molecules ranges from hundreds to millions, necessitating a large state space for neural network representation. To reduce the number of states, we employed coordinate embedding to transform state coordinate values into vectorized representations. This embedding process involves base conversion of the coordinate value into a binary or decimal number, followed by the creation of a vector with each element corresponding to a digit in the number. In the case of a light-controlled gene expression system, to achieve efficient computations, we constrained the vector sizes for certain coordinates to automatically account for state constraints, such as the number of genes. This reduction in vector sizes also decreased the number of species. Training was conducted using a trajectory ensemble dataset comprising 0.25 million trajectories. To generate this ensemble, 256 different parameter sets were initially sampled using a quasi-Monte Carlo method with the Sobol sequence. Subsequently, 1,000 trajectories were sampled for each

parameter set using Gillespie’s algorithm. The model underwent training for 40 epochs, totaling 80 hours on a cloud server equipped with 4 NVIDIA GeForce RTX 4090 GPUs.

Obtaining posterior probability with the omniscient neural network model

To estimate the posterior probability of each set of rate constants, we posited a fundamental assumption: the cells are entrapped randomly within the microfluidic chip’s cavities. The fluorescence emissions emanating from these cells follow a distribution dictated by the stochastic dynamics inherent to the optical-controlled gene expression system. The trained neural network model provides an accurate approximation for the state joint distribution given the rate constants and the time value $\hat{p}^\theta(\mathbf{x}_t|\boldsymbol{\sigma}, \mathbf{x}_0, t_0)$, $p(\mathbf{x}|\boldsymbol{\sigma})$ for short. For parameter inferring, we used the Metropolis-Hastings algorithm with the state likelihood provided by the neural network model. At Monte Carlo step s , we used a Gaussian kernel for generating the next step proposal rate parameters $\boldsymbol{\sigma}_{s+1} = \boldsymbol{\sigma}_s + \mathbf{l} \cdot \mathcal{N}(0, \Sigma)$, where covariance matrix Σ is diagonal for controlling the Monte Carlo step size, and \mathbf{l} is the scale factor. Since the symmetry of Gaussian kernels, it is evident that $p(\boldsymbol{\sigma}_{s+1}|\boldsymbol{\sigma}_s) = p(\boldsymbol{\sigma}_s|\boldsymbol{\sigma}_{s+1})$. We also use a Gamma probability density function to account for the prior knowledge of $\boldsymbol{\sigma}$. The accepting criterion for Metropolis-Hastings algorithm is then

$$\gamma = \frac{p(\boldsymbol{\sigma}_{s+1}|\mathbf{x})}{p(\boldsymbol{\sigma}_s|\mathbf{x})} \cdot \frac{p(\boldsymbol{\sigma}_s|\boldsymbol{\sigma}_{s+1})}{p(\boldsymbol{\sigma}_{s+1}|\boldsymbol{\sigma}_s)} = \frac{p(\mathbf{x}|\boldsymbol{\sigma}_{s+1})\Gamma(\boldsymbol{\sigma}_{s+1})}{p(\mathbf{x}|\boldsymbol{\sigma}_s)\Gamma(\boldsymbol{\sigma}_s)}$$

which is the product of the ratio of the joint likelihoods and the ratio of the prior probability. The movement from the original rate parameters $\boldsymbol{\sigma}_s$ to the new rate parameters $\boldsymbol{\sigma}_{s+1}$ is only allowed with the probability $\min(1, \gamma)$. During the Monte Carlo sampling, n states are randomly chosen from the observed trajectories that correspond to different times. The accepting criterion can then be written as:

$$\gamma = \prod_i^n \frac{p(x_i|\boldsymbol{\sigma}_{s+1})}{p(x_i|\boldsymbol{\sigma}_s)} \cdot \frac{\Gamma(\boldsymbol{\sigma}_{s+1})}{\Gamma(\boldsymbol{\sigma}_s)}$$

The trained neural network model was then used to approximate $p(x_i|\boldsymbol{\sigma}_s, t_i)$ for estimating γ :

$$\gamma \approx \exp \left[\sum_i^n (\ln \hat{p}_\theta(x_i|\boldsymbol{\sigma}_{s+1}, t_i) - \ln \hat{p}_\theta(x_i|\boldsymbol{\sigma}_s, t_i)) \right] \cdot \frac{\Gamma(\boldsymbol{\sigma}_{s+1})}{\Gamma(\boldsymbol{\sigma}_s)}$$

Data & code availability

The met package used in this work is available in the git repositories:

https://github.com/cbliu111/cell_seg_track_software

and

<https://github.com/cbliu111/met2>

Acknowledgments

C.-B.L. thanks the supports from the National Natural Science Foundation of China Grant 32000888, the Scientific Instrument Developing Project of the Chinese Academy of Sciences Grant YJKYYQ20180038, Jilin Province Science and Technology Development Plan Grant 20230101152JC.

Author contributions

E.L.E and C.B.L. designed the research and contributed to the experimental materials. Y.F., L.L. and C.B.L. constructed the yeast strains. C.B.L. performed the experiments, implemented the image analysis software and the MET2 package, analyzed the data, performed the numerical experiments, and wrote the original draft. J.W. provided critical suggestions, revised the manuscript, and supervised the study.

Competing interests

The authors declare no competing interests.

Correspondence

Correspondence and requests for materials should be addressed to Jin Wang.

SI Appendix

Supplementary information is provided in the SI.pdf file.

References

1. Elmentaite, R., Domínguez Conde, C., Yang, L. & Teichmann, S. A. Single-cell atlases: Shared and tissue-specific cell types across human organs. *Nature Reviews Genetics* **23**, 395–410 (2022).
2. Hilfinger, A. & Paulsson, J. Separating intrinsic from extrinsic fluctuations in dynamic biological systems. *Proceedings of the National Academy of Sciences* **108**, 12167–12172 (2011).
3. Fang, X., Kruse, K., Lu, T. & Wang, J. Nonequilibrium physics in biology. *Reviews of Modern Physics* **91**, 045004 (2019).
4. Inoue, K. *et al.* Oscillation dynamics underlie functional switching of nf- κ b for b-cell activation. *npj Systems Biology and Applications* **2**, 16024 (2016).
5. Purvis, J. E. *et al.* P53 dynamics control cell fate. *Science* **336**, 1440–1444 (2012).
6. Gupta, A. *et al.* Inferring gene regulation from stochastic transcriptional variation across single cells at steady state. *Proceedings of the National Academy of Sciences* **119**, e2207392119 (2022).
7. Kiviet, D. J. *et al.* Stochasticity of metabolism and growth at the single-cell level. *Nature* **514**, 376–379 (2014).
8. Labib, M. & Kelley, S. O. Single-cell analysis targeting the proteome. *Nature Reviews Chemistry* **4**, 143–158 (2020).
9. Munsky, B., Neuert, G. & Van Oudenaarden, A. Using gene expression noise to understand gene regulation. *Science* **336**, 183–187 (2012).
10. Boersma, S. *et al.* Multi-color single-molecule imaging uncovers extensive heterogeneity in mrna decoding. *Cell* **178**, 458–472.e19 (2019).
11. Treck, T., Lionnet, T., Shroff, H. & Lehmann, R. mrna quantification using single-molecule fish in drosophila embryos. *Nature Protocols* **12**, 1326–1348 (2017).
12. Boyden, E. S., Zhang, F., Bamberg, E., Nagel, G. & Deisseroth, K. Millisecond-timescale, genetically targeted optical control of neural activity. *Nature Neuroscience* **8**, 1263–1268 (2005).
13. Emiliani, V. *et al.* Optogenetics for light control of biological systems. *Nature Reviews Methods Primers* **2**, 55 (2022).

14. Nguyen, N. T. *et al.* Nano-optogenetic engineering of car t cells for precision immunotherapy with enhanced safety. *Nature Nanotechnology* **16**, 1424–1434 (2021).
15. Tan, P., He, L., Huang, Y. & Zhou, Y. Optophysiology: Illuminating cell physiology with optogenetics. *Physiological Reviews* **102**, 1263–1325 (2022).
16. Zhao, E. M. *et al.* Optogenetic regulation of engineered cellular metabolism for microbial chemical production. *Nature* **555**, 683–687 (2018).
17. Browning, D. F. & Busby, S. J. W. Local and global regulation of transcription initiation in bacteria. *Nature Reviews Microbiology* **14**, 638–650 (2016).
18. Sigova, A. A. *et al.* Transcription factor trapping by rna in gene regulatory elements. *Science* **350**, 978–981 (2015).
19. Schier, A. C. & Taatjes, D. J. Structure and mechanism of the rna polymerase ii transcription machinery. *Genes & Development* **34**, 465–488 (2020).
20. Jones, D. L., Brewster, R. C. & Phillips, R. Promoter architecture dictates cell-to-cell variability in gene expression. *Science* **346**, 1533–1536 (2014).
21. Abner, K., Aaviksaar, T., Adamberg, K. & Vilu, R. Single-cell model of prokaryotic cell cycle. *Journal of Theoretical Biology* **341**, 78–87 (2014).
22. Kamarthapu, V. *et al.* ppgpp couples transcription to dna repair in *e. coli*. *Science* **352**, 993–996 (2016).
23. Bintu, L. *et al.* Dynamics of epigenetic regulation at the single-cell level. *Science* **351**, 720–724 (2016).
24. Orphanides, G. & Reinberg, D. A unified theory of gene expression. *Cell* **108**, 439–451 (2002).
25. Sohmen, D. *et al.* Structure of the bacillus subtilis 70s ribosome reveals the basis for species-specific stalling. *Nature Communications* **6**, 6941 (2015).
26. Louder, R. K. *et al.* Structure of promoter-bound tfiid and model of human pre-initiation complex assembly. *Nature* **531**, 604–609 (2016).
27. Alberts, B. *Molecular Biology of the Cell* (CRC Press, an imprint of Garland Science, Boca Raton, FL, 2017), sixth edition edn.
28. Cramer, P. Organization and regulation of gene transcription. *Nature* **573**, 45–54 (2019).

29. Chen, J., Boyaci, H. & Campbell, E. A. Diverse and unified mechanisms of transcription initiation in bacteria. *Nature Reviews Microbiology* **19**, 95–109 (2021).
30. Girbig, M., Misiaszek, A. D. & Müller, C. W. Structural insights into nuclear transcription by eukaryotic dna-dependent rna polymerases. *Nature Reviews Molecular Cell Biology* **23**, 603–622 (2022).
31. Ay, A. & Arnosti, D. N. Mathematical modeling of gene expression: A guide for the perplexed biologist. *Critical Reviews in Biochemistry and Molecular Biology* **46**, 137–151 (2011).
32. Rué, P. & Garcia-Ojalvo, J. Modeling gene expression in time and space. *Annual Review of Biophysics* **42**, 605–627 (2013).
33. Shahrezaei, V. & Swain, P. S. Analytical distributions for stochastic gene expression. *Proceedings of the National Academy of Sciences* **105**, 17256–17261 (2008).
34. Elowitz, M. B., Levine, A. J., Siggia, E. D. & Swain, P. S. Stochastic gene expression in a single cell. *Science* **297**, 1183–1186 (2002).
35. Thattai, M. & van Oudenaarden, A. Intrinsic noise in gene regulatory networks. *Proceedings of the National Academy of Sciences* **98**, 8614–8619 (2001).
36. Beaumont, M. A. Approximate bayesian computation. *Annual Review of Statistics and Its Application* **6**, 379–403 (2019).
37. Gillespie, D. T. Exact stochastic simulation of coupled chemical reactions. *The Journal of Physical Chemistry* **81**, 2340–2361 (1977).
38. Kilic, Z., Schweiger, M., Moyer, C., Shepherd, D. & Pressé, S. Gene expression model inference from snapshot rna data using bayesian non-parametrics. *Nature Computational Science* **3**, 174–183 (2023).
39. Nash, A. I. *et al.* Structural basis of photosensitivity in a bacterial light-oxygen-voltage/helix-turn-helix (lov-hth) dna-binding protein. *Proceedings of the National Academy of Sciences* **108**, 9449–9454 (2011).
40. Lee, J. B., Caywood, L. M., Lo, J. Y., Levering, N. & Keung, A. J. Mapping the dynamic transfer functions of eukaryotic gene regulation. *Cell Systems* **12**, 1079–1093.e6 (2021).
41. Shimizu-Sato, S., Huq, E., Tepperman, J. M. & Quail, P. H. A light-switchable gene promoter system. *Nature Biotechnology* **20**, 1041–1044 (2002).

42. Li, H., Burgie, E. S., Gannam, Z. T. K., Li, H. & Vierstra, R. D. Plant phytochrome b is an asymmetric dimer with unique signalling potential. *Nature* **604**, 127–133 (2022).
43. Smith, R. W. *et al.* Interactions between phyb and pif proteins alter thermal reversion reactions *in vitro*. *Photochemistry and Photobiology* **93**, 1525–1531 (2017).
44. Klose, C. *et al.* Systematic analysis of how phytochrome b dimerization determines its specificity. *Nature Plants* **1**, 15090 (2015).
45. Castillon, A., Shen, H. & Huq, E. Phytochrome interacting factors: Central players in phytochrome-mediated light signaling networks. *Trends in Plant Science* **12**, 514–521 (2007).
46. Smith, H. & Jackson, G. M. Rapid phytochrome regulation of wheat seedling extension: Light pretreatment extends coupling time, increases response lag, and decreases light sensitivity. *Plant Physiology* **84**, 1059–1062 (1987).
47. Khmelinskii, A. *et al.* Tandem fluorescent protein timers for in vivo analysis of protein dynamics. *Nature Biotechnology* **30**, 708–714 (2012).
48. Motta-Mena, L. B. *et al.* An optogenetic gene expression system with rapid activation and deactivation kinetics. *Nature Chemical Biology* **10**, 196–202 (2014).
49. Benzinger, D. & Khammash, M. Pulsatile inputs achieve tunable attenuation of gene expression variability and graded multi-gene regulation. *Nature Communications* **9**, 3521 (2018).
50. Li, F.-W. *et al.* Phytochrome diversity in green plants and the origin of canonical plant phytochromes. *Nature Communications* **6**, 7852 (2015).
51. Legris, M., Ince, Y. Ç. & Fankhauser, C. Molecular mechanisms underlying phytochrome-controlled morphogenesis in plants. *Nature Communications* **10**, 5219 (2019).
52. Klose, C., Nagy, F. & Schäfer, E. Thermal reversion of plant phytochromes. *Molecular Plant* **13**, 386–397 (2020).
53. Matsushita, T., Mochizuki, N. & Nagatani, A. Dimers of the n-terminal domain of phytochrome b are functional in the nucleus. *Nature* **424**, 571–574 (2003).
54. Burgie, E. S. *et al.* Differing biophysical properties underpin the unique signaling potentials within the plant phytochrome photoreceptor families. *Proceedings of the National Academy of Sciences* **118**, e2105649118 (2021).

55. Chen, E., Lapko, V. N., Lewis, J. W., Song, P.-S. & Kliger, D. S. Mechanism of native oat phytochrome photoreversion: A time-resolved absorption investigation. *Biochemistry* **35**, 843–850 (1996).
56. Björling, A. *et al.* Structural photoactivation of a full-length bacterial phytochrome. *Science Advances* **2**, e1600920 (2016).
57. Sineshchekov, V. A. Evidence for the existence of two phytochrome a populations. *Journal of Photochemistry and Photobiology B: Biology* **28**, 53–55 (1995).
58. Schmidt, P. *et al.* The complexity of the p_r to p_{fr} phototransformation kinetics is an intrinsic property of native phytochrome*. *Photochemistry and Photobiology* **68**, 754–761 (1998).
59. Burgie, E. S. *et al.* Crystallographic and electron microscopic analyses of a bacterial phytochrome reveal local and global rearrangements during photoconversion. *Journal of Biological Chemistry* **289**, 24573–24587 (2014).
60. Takala, H., Björling, A., Linna, M., Westenhoff, S. & Ihalainen, J. A. Light-induced changes in the dimerization interface of bacteriophytochromes. *Journal of Biological Chemistry* **290**, 16383–16392 (2015).
61. Hennig, L. & Schäfer, E. Both subunits of the dimeric plant photoreceptor phytochrome require chromophore for stability of the far-red light-absorbing form. *Journal of Biological Chemistry* **276**, 7913–7918 (2001).
62. Sweere, U. *et al.* Interaction of the response regulator arr4 with phytochrome b in modulating red light signaling. *Science* **294**, 1108–1111 (2001).
63. Ni, M., Tepperman, J. M. & Quail, P. H. Pif3, a phytochrome-interacting factor necessary for normal photoinduced signal transduction, is a novel basic helix-loop-helix protein. *Cell* **95**, 657–667 (1998).
64. Golonka, D. *et al.* Deconstructing and repurposing the light-regulated interplay between arabidopsis phytochromes and interacting factors. *Communications Biology* **2**, 448 (2019).
65. Nagano, S. *et al.* Structural insights into photoactivation and signalling in plant phytochromes. *Nature Plants* **6**, 581–588 (2020).
66. Yoo, C. Y. *et al.* Direct photoresponsive inhibition of a p53-like transcription activation domain in pif3 by arabidopsis phytochrome b. *Nature Communications* **12**, 5614 (2021).
67. Weber, M. F. & Frey, E. Master equations and the theory of stochastic path integrals. *Reports on Progress in Physics* **80**, 046601 (2017).

68. Cao, Y. & Liang, J. Adaptively biased sequential importance sampling for rare events in reaction networks with comparison to exact solutions from finite buffer dcme method. *The Journal of Chemical Physics* **139**, 025101 (2013).
69. Pelechano, V., Chávez, S. & Pérez-Ortín, J. E. A complete set of nascent transcription rates for yeast genes. *PLoS ONE* **5**, e15442 (2010).
70. Schwanhäusser, B. *et al.* Global quantification of mammalian gene expression control. *Nature* **473**, 337–342 (2011).
71. Sharma, A. K. *et al.* A chemical kinetic basis for measuring translation initiation and elongation rates from ribosome profiling data. *PLOS Computational Biology* **15**, e1007070 (2019).
72. Manavalan, B., Kuwajima, K. & Lee, J. Pfdb: A standardized protein folding database with temperature correction. *Scientific Reports* **9**, 1588 (2019).
73. Guerra, P., Vuilleminot, L.-A., Rae, B., Ladyhina, V. & Milias-Argeitis, A. Systematic *in vivo* characterization of fluorescent protein maturation in budding yeast. *ACS Synthetic Biology* **11**, 1129–1141 (2022).
74. Timms, R. T. *et al.* A glycine-specific n-degron pathway mediates the quality control of protein *n*-myristoylation. *Science* **365**, eaaw4912 (2019).
75. Varshavsky, A. N-degron and c-degron pathways of protein degradation. *Proceedings of the National Academy of Sciences* **116**, 358–366 (2019).
76. Gligorovski, V., Sadeghi, A. & Rahi, S. J. Multidimensional characterization of inducible promoters and a highly light-sensitive lov-transcription factor. *Nature Communications* **14**, 3810 (2023).
77. Taniguchi, Y. *et al.* Quantifying *e. coli* proteome and transcriptome with single-molecule sensitivity in single cells. *Science* **329**, 533–538 (2010).
78. Bar-Even, A. *et al.* Noise in protein expression scales with natural protein abundance. *Nature Genetics* **38**, 636–643 (2006).
79. Shahrezaei, V. & Swain, P. S. The stochastic nature of biochemical networks. *Current Opinion in Biotechnology* **19**, 369–374 (2008).
80. Shao, J. *et al.* Smartphone-controlled optogenetically engineered cells enable semiautomatic glucose homeostasis in diabetic mice. *Science Translational Medicine* **9**, eaal2298 (2017).

81. Pédelacq, J.-D., Cabantous, S., Tran, T., Terwilliger, T. C. & Waldo, G. S. Engineering and characterization of a superfolder green fluorescent protein. *Nature Biotechnology* **24**, 79–88 (2006).
82. Li, Y. *et al.* A programmable fate decision landscape underlies single-cell aging in yeast. *Science* **369**, 325–329 (2020).
83. Kirillov, A. *et al.* Segment anything (2023). [2304.02643](#).

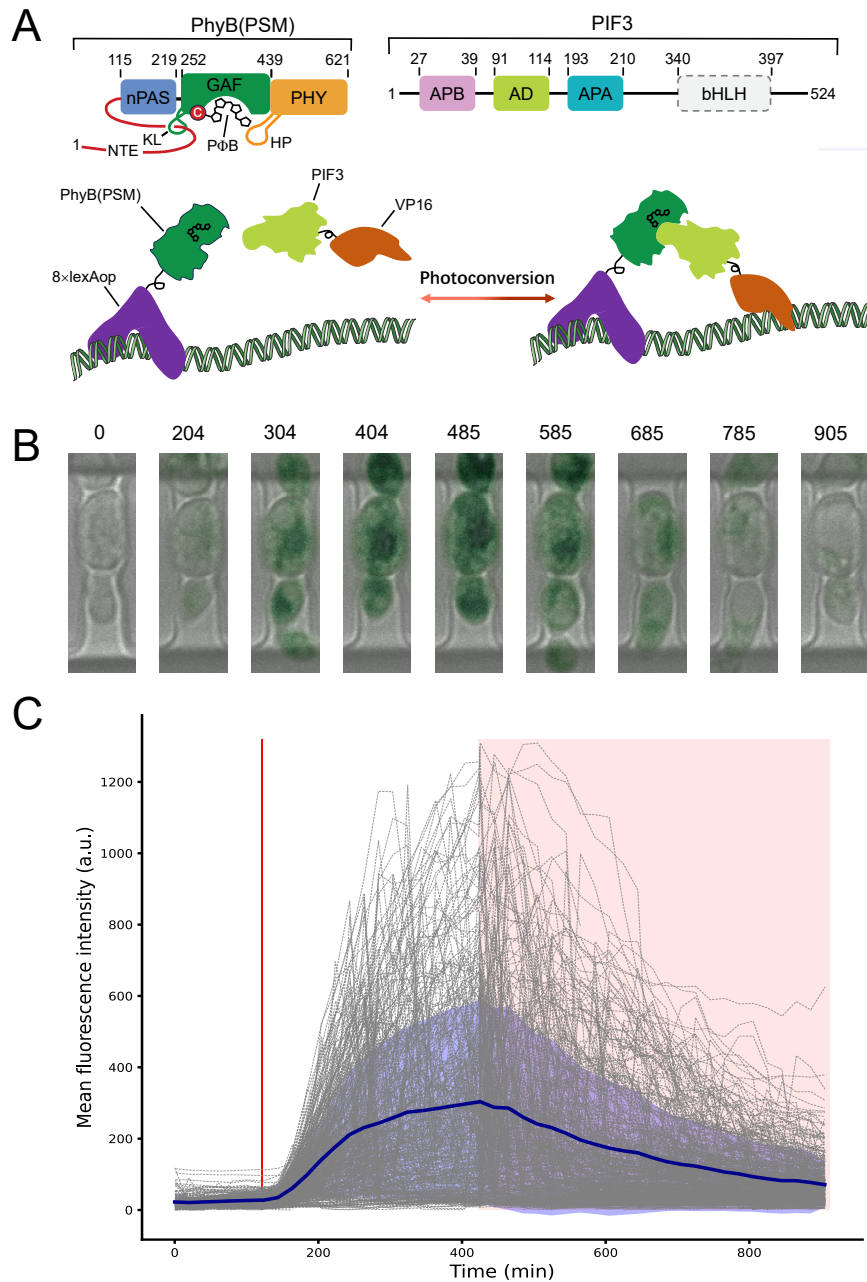


Fig. 1 Perturbing gene expression with light. (A) Schematic of the PhyB-based optical-controlled gene expression system. (B) Representative time-lapse images of light-activated yeast cell incubated in traps of microfluidic chip channels. Signal of sGFP expression is shown with green colors. The capturing times of the images is labeled on top of these images with unit minutes. (C) Mean fluorescence intensity of cells as function of observation time. Intensity of each cell is plotted as light-gray dotted lines, mean value of these trajectories is denoted by the solid blue line and light blue region indicates the standard deviation. Red light activation is represented by red pulse starting at 120 min and lasts 2 mins. Far-red light deactivation is represented by light-red box starting at 422 min and lasts 490 mins.

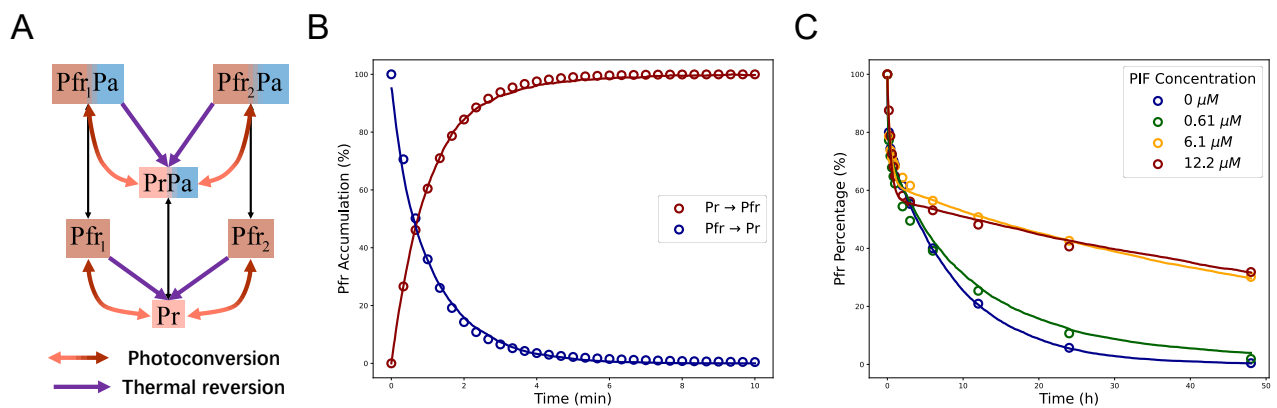


Fig. 2 Minimized model for photoconversion and thermal reversion dynamics of phytochromes. (A) Schematic of the state conversion model. Pr and Pfr state are labeled with light and dark red, respectively. Fragment of PIF was denoted as Pa. In the minimized model, dimer photoconversion and transformation between Pfr1 and Pfr2 state are omitted. (B) Fitting of stochastic reaction networks to the photoconversion processes. Experimental data representing the photoconversion of PhyB(NT) at 25 °C (empty circle) were obtained from Figure 2 of⁵⁴. (C) Fitting of stochastic reaction networks to the thermal reversion processes. Experimental data representing the thermal reversion of PhyB(NT) under different concentration of PIFs at 22 °C (empty circle) were obtained from Figure 3 of⁴³. The system was photo-activated under red light for 10 min before darkness for observation. The photoconversion rates obtained from (B) was used in the fitting of thermal reversion rates since the photoconversion rates are not sensitive to temperature alterations^{52,54}.

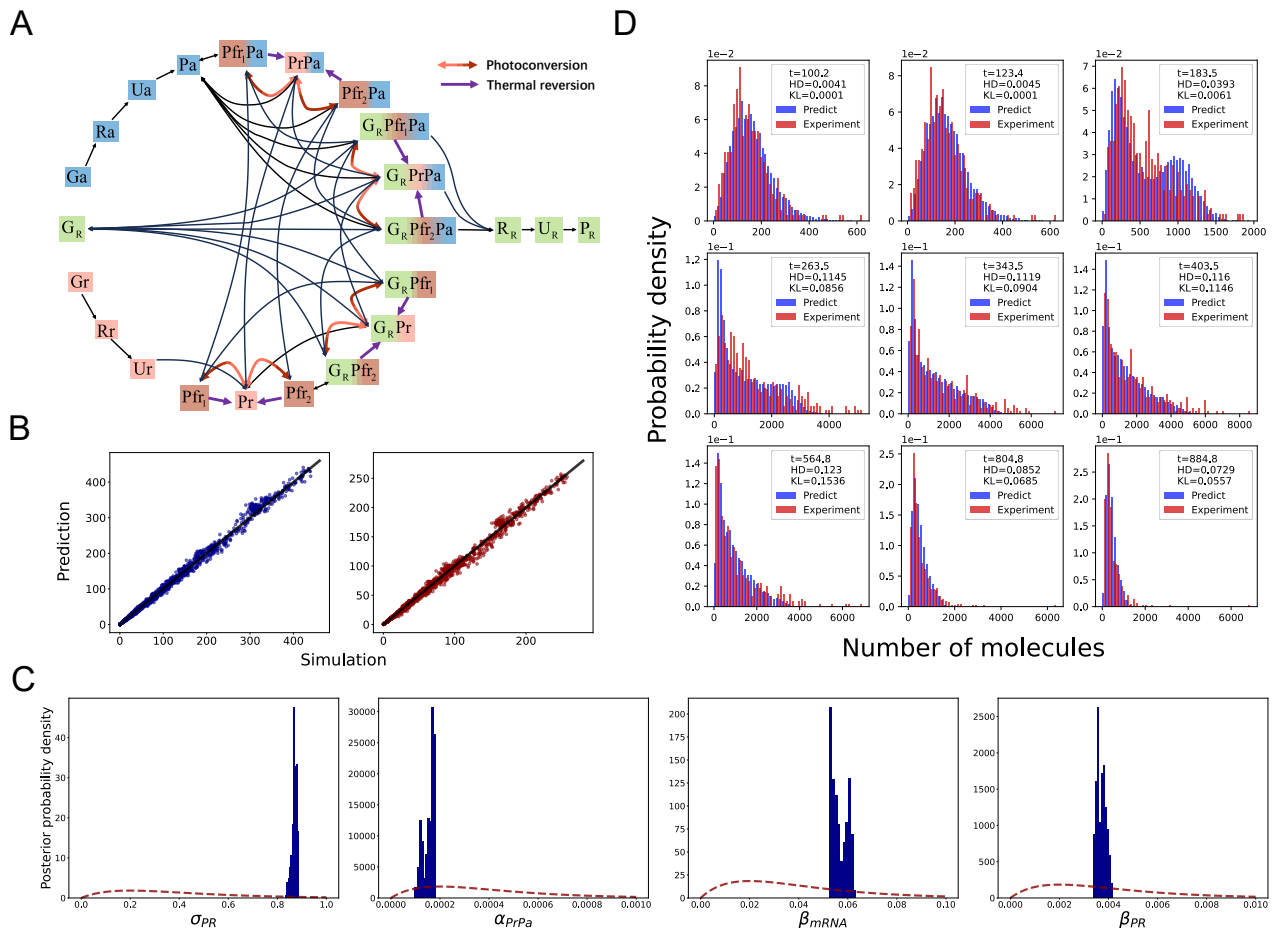


Fig. 3 Stochastic modeling and parameter inference of optical-controlled gene expression system. (A) Stochastic modeling of the PhyB-based optical-controlled gene expression system. Gene, mRNA, immature protein are labeled with capital letters “G”, “R” and “U” for each species, respectively. PhyB, PIF and fluorescence reporter are represented by letter “r”, “a” and “R”, respectively. e.g. G_R represents the gene of fluorescence reporter, and $G_R P_{f_{r1}} Pa$ is the trimmer comprised by gene of fluorescence report, the activated Pf_{r1} and PIF3. Pr and Pfr state are labeled with light and dark red, respectively, as in Fig. 2. Fluorescence reporter and of PIF was denoted as Pa. The reporter gene (G_R) In the minimized model, dimer photoconversion and transformation between Pf_{r1} and Pf_{r2} state are omitted. (B) Validation of the trained neural network for prediction of population mean and standard deviations of the reporter protein for 2,400 parameter combinations. Means and standard deviations are calculated using 1,000 samples from either neural network predictions or stochastic simulation results. (C) Posterior probability distributions obtained through Markov Chain Monte Carlo sampling for σ_{PR} , α_{PrPa} , β_{mRNA} and β_{PR} . Prior distributions are shown by dashed dark red lines. (D) Histograms of predicted reporter protein number compared to experimental results.

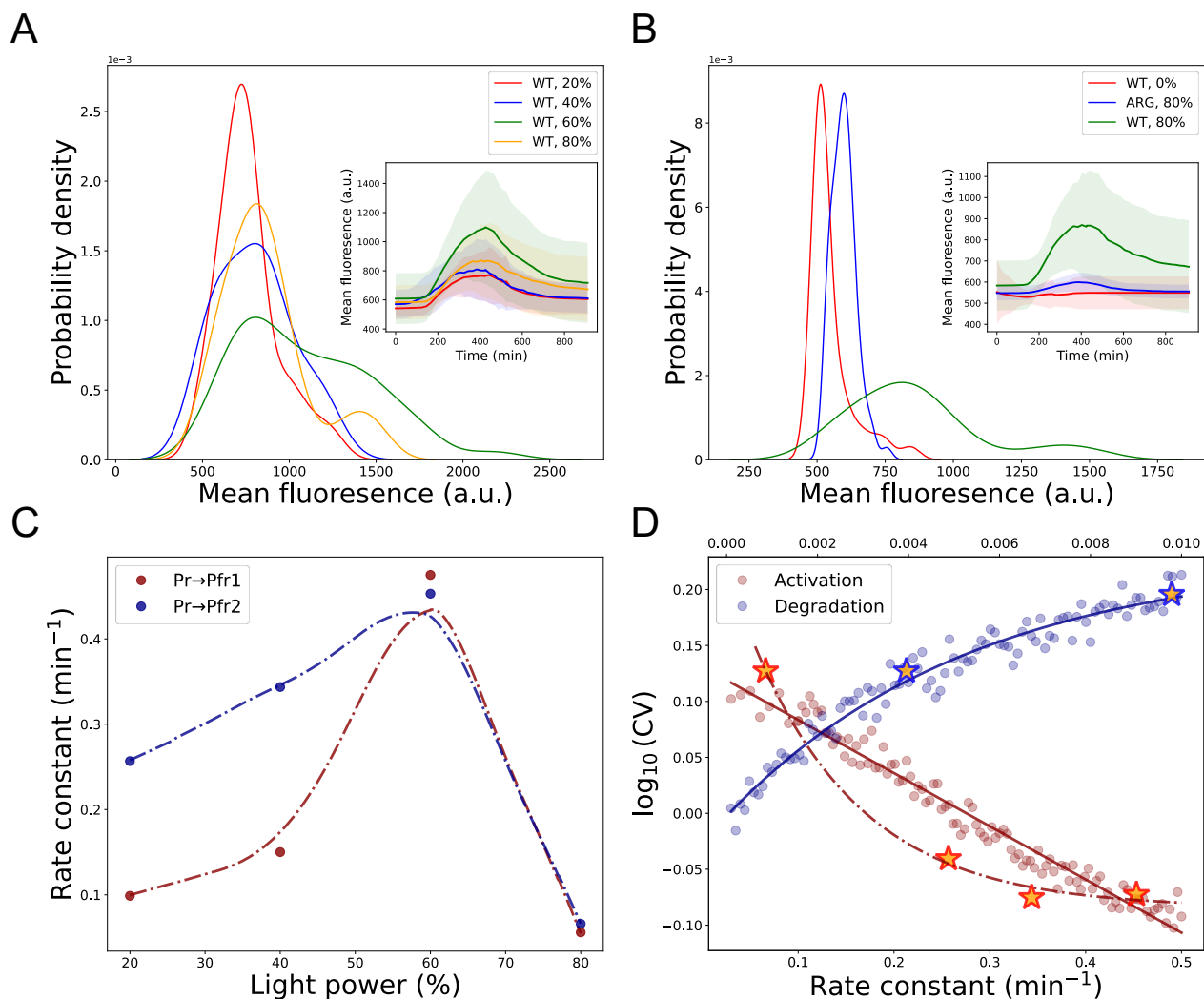


Fig. 4 Modulation of fluctuations with optical-controlled gene expression system. (A) Steady-state probability distributions corresponding to different activation light intensities. (B) Steady-state probability distributions of wild-type and N-terminal mutagenesis fluorescent reporter. The inset figures in (A) and (B) showed the change of mean fluorescence intensities along with observation times. (C) Dependency of rate constants on activation light intensities. The inferring rate constants are represented as solid dots, and dash-dot lines show the smoothed spline interpolation of the data. (D) Dependency of logarithm of coefficient of variations (CV) on activation and degradation rate constants (ticks are shown in lower and upper x-axes). The solid dots represent the results obtained from stochastic simulations, and colored stars denote the experimental results. The red solid line indicates a linear fitting of the rate constant ($\text{Pr} \rightarrow \text{Pfr}_2$) to the logarithm of CV and blue solid line indicates an exponentially fitting of the degradation rate constant to logarithm of CV. The red dash-dot line is an exponentially fitting of the rate constant to the logarithm of CV. Each experimental result represents a collection of mean fluorescent intensities from about 20,000 cells.